The thermal analysis of cutting/grinding processes by meshless finite block method

J.J. Yang [1], Z.X. Wang[2*†], O.B. Adetoro[3], P.H. Wen[2*] and C.G. Bailey[2]

[1]*School of Traffic and Transportation Engineering, Changsha University of Technology and Science, China*

[2]*School of Engineering and Materials Science, Queen Mary University of London, London E1 4NS, UK*

[3]*College of Engineering, Design and Physical Sciences, Brunel University, London UB8 3PH, UK*

Abstract

Development of the Finite Block Method (FBM) is presented, with the introduction of infinite elements for the first time, for predicting stationary and transient heat conduction in cutting/grinding processes. Utilizing the Lagrange series the first order partial differential matrix is derived, adopting a mapping technique, followed by the construction of the higher order derivative matrix. For linear stationary heat conductivity three free parameters including the velocity of the workpiece, the cooling coefficient and the inclined angle of the contact zone, together with their effects on temperature, are observed. For the transient heat conduction study, the Laplace transformation method and Durbin's inverse technique are employed. Numerical solutions are discussed and comparisons made with the finite element method and analytical solutions, demonstrating the accuracy and convergence of the finite block method.

Key words: finite block method, mapping technique and differential matrix, infinite element, Lagrange series interpolation, cutting and grinding processes, heat transfer.

* Corresponding author: Email: zixuan.wang@qmul.ac.uk (Z.X.Wang), p.h.wen@qmul.ac.uk (P.H.Wen)

† on leave from the School of Mechanical Engineering and Automation, Northeastern University, China

1. Introduction

In the past forty years, many cutting/grinding heat models have been proposed and investigated [1-3]. Accurate prediction of heat transfer is important since high temperatures can lead to surface thermal damage during the cutting/grinding process. Most of the heat is generated at the interface during the grinding process due to friction [4], which can dissipate in four ways; by transferring heat to the workpiece, grinding wheel, coolant and chips. In 1942 Jaeger [5] systematically studied, for the first time, the temperature distribution between sliding contacts observing the movement of heat. Different heat source distribution (the band heat source and the rectangular heat source) and different moving times (a finite time and an infinite time) were investigated by Jaeger and analytical models developed. Until recently, most of the thermal models are based on Jaeger's original moving heat source theory [1].   However, due to the complex nature of most grinding techniques, numerical simulation becomes more important and effective. Shen *et al*. [7] developed a two-dimensional heat transfer model to investigate the grinding process based on the Finite Difference Method (FDM) and compared their results with previous traditional models for validation. By using FDM, a three-dimensional grinding model was proposed by Wang *et al*. [8] in order to determine the temperature field. The Finite Element Method (FEM) by Dawson and Malkin [9] was applied with a moving heat source in order to discretize the differential equation. The contact area between the wheel and the workpiece (or shear plane) is considered as the location of the heat source, which moves along the surface of a semi-infinite solid. The numerical results can be used to predict the grinding zone or shear plane temperature. Moulik *et al.* [10] conducted an analysis of temperature and thermal stress using a transient heat conduction model using FEM, which was validated using an analytical solution. Gu *et al*. [11] conducted the temperature numerical analysis in the workpiece and grinding wheel using the Petrov-Galerkin weighted residual FEM. In addition, the independent variable of time was discretized by applying an implicit integration scheme.

Mahdi *et al*. [6] obtained the temperature distribution and phase transformation in a workpiece using the finite element software ADINA. Anderson *et al.* [12] applied ANSYS and results were compared with a simplified analytical solution. It was shown that the numerical model provided more accurate results compared to the simplified analytical models for the grinding process with a large depth of cut. Parente *et al*. [13] computed the temperature field of a workpiece using ABAQUS, taking the cooling effect of liquid into consideration, with the

numerical predictions comparing well with experiment results. The heat transfer problem with a moving heat source along the surface was studied analytically and numerically by Li and Li [14]. A series representation of the solution for creep-feed grinding was calculated numerically by Gonzalez-Santander [15].

In recent years mesh reduction approaches, including the boundary element method and the meshless method, have become popular due to them being highly adaptable and low cost associated with preparing input data and analyzing output results within the numerical models [16,17,18]. Li *et al* [19] modeled the grinding wheel by the Discrete Element Method (DEM) and analyzed the effect of applied loads on the damage of the wheel. Experiments were conducted to validate the results of the simulation. Shimizu *et al*. [20] investigated the mechanism of material removal and material deformation in the grinding process by the Molecular Dynamics Method (MDM) for the aluminum atom and carbon atom. Two different Morse potentials are applied to describe the interaction between aluminum atoms, and between an aluminum atom and a carbon atom. By using FEM, Nguyen and Butler [21,22] modeled the grinding wheel and generated the processed workpiece surface. The data of the wheel topography was obtained in Gaussian field, and therefore the desired topography in non-Gaussian field is obtained using the inverse technique. The model of wheel topography is described by topography height and summit curvature in every grid, rather than the shape or position of abrasive grains. An algorithm to establish the relationship between the summit curvature of the wheel topographical point and the workpiece material removal mode (rub, plough or cut) was proposed. The surface of the workpiece was updated according to the estimated material removal mode for every topographical point until the final processed surface was achieved. The simulated results were consistent with that of experiments.

The finite block method–a meshless method–based on the point collocation method was developed firstly to solve the heat conduction problem in the functionally graded media and anisotropic materials by Li and Wen [23]. Recently, this method was developed to analyse nonlinear elasticity including frictionless/friction contact by Wen *et al* [24] and Li *et al* [25,26]. The essential characteristics of the FBM is that the domain is divided into a few blocks and the partial differential matrices are applied to each block. Therefore, the degree of accuracy should be higher than other meshless methods due to the fact that all stress components are continuous along the interface between two blocks. In the present paper, a heat conduction numerical

solution is presented for the problem of a moving band source of heat q_0 on a semi-infinite solid, inclined at angle ϕ to its direction of motion, with material disappearing as the heat source passes. To demonstrate the accuracy and efficiency of the FBM, a numerical example is presented and comparisons are made with both finite element method [9] and analytical solution [5].

2. Two dimension differential matrices

FBM is a meshless collocation method and well developed using the Lagrange interpolation and mapping technique [24]. Consider a set of nodes as shown in Figure 1(a) in the normalised domain with the nodes collocated at $\xi_\alpha^{(k)}$, $\alpha = 1,2$, $k = 1,2,...,N_\alpha$, where N_α is the number of node along axis ξ_α. By using Lagrange polynomials, a function $u(\xi_1,\xi_2)$ can be interpolated by

$$u(\xi_1,\xi_2) = \sum_{i=1}^{N_1}\sum_{j=1}^{N_2} F_1(\xi_1,\xi_1^{(i)})F_2(\xi_2,\xi_2^{(j)})u^{(k)} \tag{1}$$

where

$$F_\alpha(\xi_\alpha,\xi_\alpha^{(i)}) = \prod_{\substack{m=1\\m\neq i}}^{N_\alpha} \frac{(\xi_\alpha - \xi_\alpha^{(m)})}{(\xi_\alpha^{(i)} - \xi_\alpha^{(m)})} \tag{2}$$

$u^{(k)}$ is nodal value, $k = (j-1)\times N_1 + i$, as shown in Figure 1(a) and the number of node in total is $M = N_1 \times N_2$. The partial differential is obtained straightaway

$$\frac{\partial u}{\partial \xi_1} = \sum_{i=1}^{N_1}\sum_{j=1}^{N_2} \frac{\partial F_1(\xi_1,\xi_1^{(i)})}{\partial \xi_1} F_2(\xi_2,\xi_2^{(j)})u^{(k)} \tag{3}$$

and

$$\frac{\partial u}{\partial \xi_2} = \sum_{i=1}^{N_1}\sum_{j=1}^{N_2} \frac{\partial F_2(\xi_2,\xi_2^{(j)})}{\partial \xi_2} F_1(\xi_1,\xi_1^{(i)})u^{(k)} \tag{4}$$

In order to derive the partial derivatives in physical domain, the mapping technique should be utilized. Two-dimensional area Ω in the Cartesian coordinate (x_1,x_2) can be mapped into a square Ω' in the domain (ξ_1,ξ_2) $|\xi_1|\leq 1; |\xi_2|\leq 1$ shown in Figure 1(b) using quadratic shape functions, same as the finite element method, as below

$$N_i(\xi_1,\xi_2) = \frac{1}{4}(1+\xi_1^{(i)}\xi_1)(1+\xi_2^{(i)}\xi_2)(\xi_1^{(i)}\xi_1+\xi_2^{(i)}\xi_2-1) \quad \text{for} \quad i=1,2,3,4 \tag{5}$$

$$N_i(\xi_1,\xi_2) = \frac{1}{2}(1-\xi_1^2)(1+\xi_2^{(i)}\xi_2) \qquad\qquad \text{for} \quad i=5,7 \tag{6}$$

$$N_i(\xi_1,\xi_2) = \frac{1}{2}(1-\xi_2^2)(1+\xi_1^{(i)}\xi_1) \qquad\qquad \text{for} \quad i=6,8 \tag{7}$$

(a)   (b)
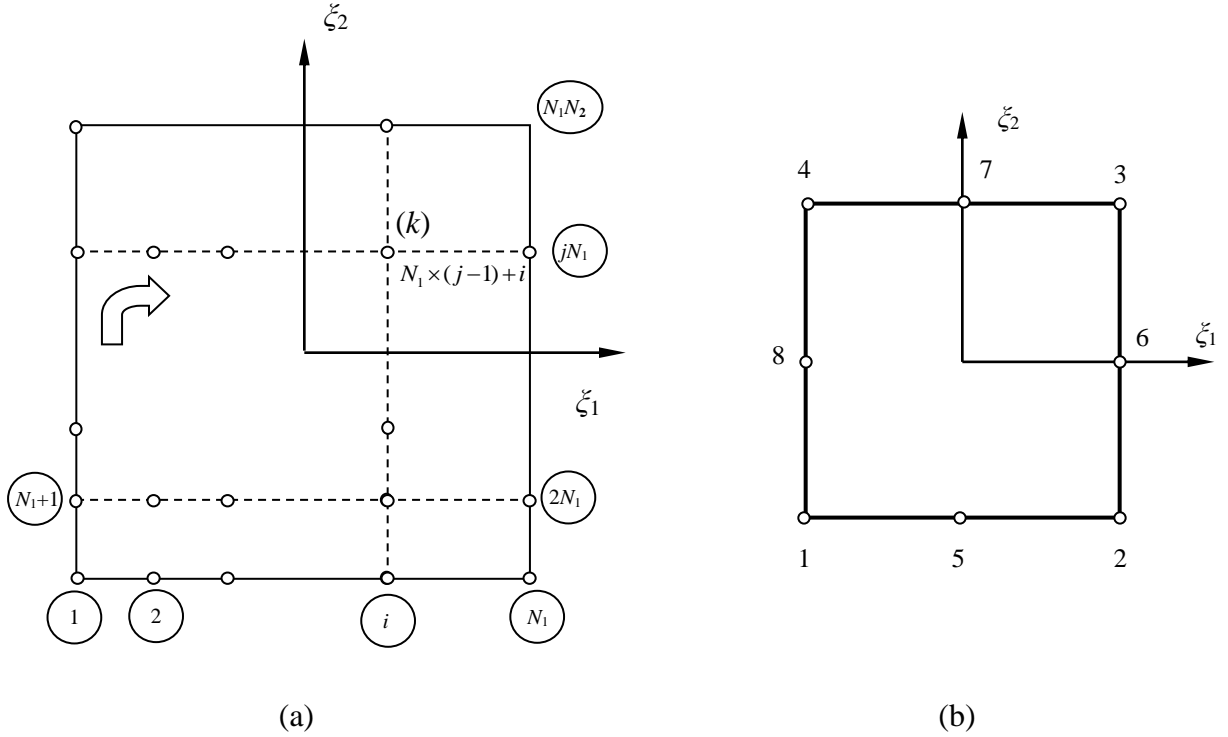
Figure 1. Two-dimensional node distribution in mapping domain: (a) the local number system of node; (b) mapping domain with 8 seeds.

Therefore, the mapping of the domain can be applied with shape functions used in FEM, i.e. the coordinate transformation is written as following

$$x_\alpha = \sum_{k=1}^{8} N_k(\xi_1,\xi_2)x_\alpha^{(k)}, \qquad \alpha=1,2 \tag{8}$$

where $(x_1^{(k)}, x_2^{(k)})$ presents the coordinate of seed k in the physical domain. Therefore, the first order partial differentials of function $u(x_1,x_2)$ gives

$$\frac{\partial u}{\partial x_1} = \frac{1}{J}\left(\beta_{11}\frac{\partial u}{\partial \xi_1}+\beta_{12}\frac{\partial u}{\partial \xi_2}\right), \quad \frac{\partial u}{\partial x_2} = \frac{1}{J}\left(\beta_{21}\frac{\partial u}{\partial \xi_1}+\beta_{22}\frac{\partial u}{\partial \xi_2}\right), \tag{9}$$

where

$$\beta_{11} = \frac{\partial x_2}{\partial \xi_2}, \beta_{12} = -\frac{\partial x_2}{\partial \xi_1}, \beta_{21} = -\frac{\partial x_1}{\partial \xi_2}, \beta_{22} = \frac{\partial x_1}{\partial \xi_1}, \ J = \beta_{22}\beta_{11} - \beta_{21}\beta_{12} \tag{10}$$

Thus, the first partial derivatives are obtained

$$\frac{\partial u}{\partial x_1} = \frac{1}{J}\sum_{i=1}^{N_1}\sum_{j=1}^{N_2}\left[\beta_{11}\frac{\partial F_1(\xi_1,\xi_1^{(i)})}{\partial \xi_1}F_2(\xi_2,\xi_2^{(j)}) + \beta_{12}F_1(\xi_1,\xi_1^{(i)})\frac{\partial F_2(\xi_2,\xi_2^{(j)})}{\partial \xi_2}\right]u^{(k)} = \sum_{k=1}^{M}D_{1k}(\xi_1,\xi_2)u^{(k)}$$

$$\frac{\partial u}{\partial x_2} = \frac{1}{J}\sum_{i=1}^{M}\sum_{j=1}^{N}\left[\beta_{21}\frac{\partial F_1(\xi_1,\xi_1^{(i)})}{\partial \xi_1}F_2(\xi_2,\xi_2^{(j)}) + \beta_{22}F_1(\xi_1,\xi_1^{(i)})\frac{\partial F_2(\xi_2,\xi_2^{(j)})}{\partial \xi_2}\right]u^{(k)} = \sum_{k=1}^{M}D_{2k}(\xi_1,\xi_2)u^{(k)}$$

$$\tag{11}$$

For the sake of analysis convenience, the nodal evaluate of the first order partial differentials can be written in the form of vector as

$$\mathbf{u}_{,\alpha} = \mathbf{D}_\alpha\mathbf{u}, \tag{12}$$

where the nodal value of the first partial differential vector

$$\mathbf{u}_{,\alpha} = \left\{\frac{\partial u(x_1^{(1)},x_2^{(1)})}{\partial x_\alpha}, \frac{\partial u(x_1^{(2)},x_2^{(2)})}{\partial x_\alpha},...,\frac{\partial u(x_1^{(M)},x_2^{(M)})}{\partial x_\alpha}\right\}^{\mathrm{T}}. \tag{13}$$

Where the vector of the nodal value $\mathbf{u} = \{u^{(1)},u^{(2)},...,u^{(M)}\}^{\mathrm{T}}$, and the differential matrix $\mathbf{D}_\alpha = \{D_{\alpha lk}\}_{M\times M}$, in which $D_{\alpha lk} = D_{\alpha k}(\xi_1^{(l)},\xi_2^{(l)})$ $(k,l=1,2,...,M)$. In addition, the *K*-th order partial differentials with respect to both coordinates ξ_1 and ξ_2 is approximated by,

$$u_{,1...2...}^{(mn)}(\xi_1,\xi_2) = \frac{\partial^{m+n}u(\xi_1,\xi_2)}{\partial \xi_1^m \partial \xi_2^n}, \quad m+n = K \tag{14}$$

Therefore, the vectors of the higher order partial differential nodal value are interpolated, in terms of matrices $\mathbf{D}_1$ and $\mathbf{D}_2$, as

$$\mathbf{u}_{,1...2...}^{(mn)} = \mathbf{D}_1^m\mathbf{D}_2^n\mathbf{u}. \tag{15}$$

3. Two dimensional infinite elements

The infinite element, which was introduced by Wood [27], Bettess and Zienkiewicz [28] and used in the finite element method, will be utilized in the meshless approach in this paper. For two-dimensional problems, two simplest infinite elements are utilised as following:

(1) Four-nodes infinite element

In the normalised domain, the edge of right hand side $(\xi = 1)$ is mapped to infinite place as shown in Figure 2. The mapping functions are

$$N_1 = -\frac{\xi_1(1-\xi_2)}{(1-\xi_1)}, \ N_2 = \frac{(1+\xi_1)(1-\xi_2)}{2(1-\xi_1)}, \ N_3 = \frac{(1+\xi_1)(1+\xi_2)}{2(1-\xi_1)}, \ N_4 = -\frac{\xi_1(1+\xi_2)}{(1-\xi_1)} \tag{16}$$
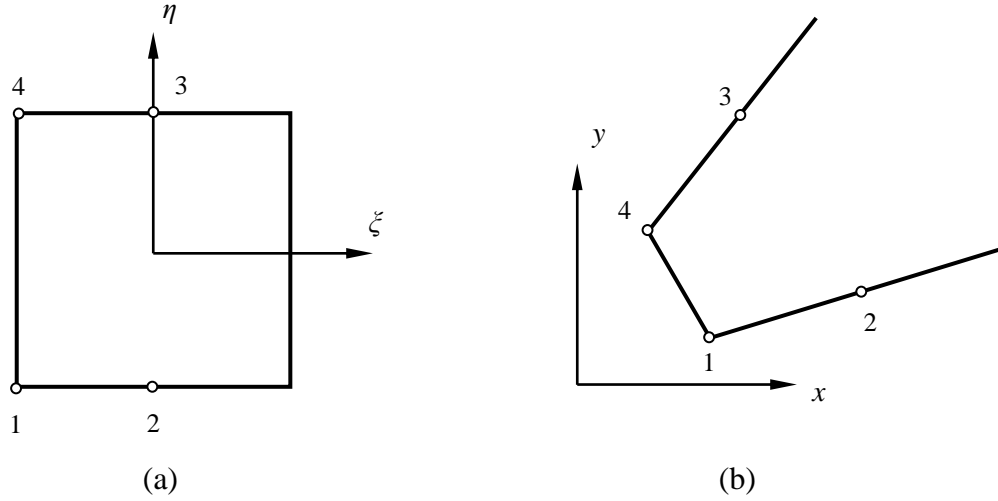

(a)   (b)

Figure 2. Four nodes mapping: (a) normalized domain; (b) physical domain.

The coordinate transform can be written as,

$$x_\alpha = \sum_{k=1}^{4} N_k(\xi_1,\xi_2)x_\alpha^{(k)}, \qquad \alpha = 1,2 \tag{17}$$

Then their partial differentials respect to ξ_1 and ξ_2 are given by

$$\frac{\partial N_1}{\partial \xi_1} = -\frac{(1-\xi_2)}{(1-\xi_1)^2}, \ \frac{\partial N_2}{\partial \xi_1} = \frac{(1-\xi_2)}{(1-\xi_1)^2}, \ \frac{\partial N_3}{\partial \xi_1} = \frac{(1+\xi_2)}{(1-\xi_1)^2}, \ \frac{\partial N_4}{\partial \xi_1} = -\frac{(1+\xi_2)}{(1-\xi_1)^2} \tag{18}$$

and

$$\frac{\partial N_1}{\partial \xi_2} = \frac{\xi_1}{(1-\xi_2)}, \ \frac{\partial N_2}{\partial \xi_2} = -\frac{(1+\xi_1)}{2(1-\xi_1)}, \ \frac{\partial N_3}{\partial \xi_2} = \frac{(1+\xi_1)}{2(1-\xi_1)}, \ \frac{\partial N_4}{\partial \xi_2} = -\frac{\xi_1}{(1-\xi_1)}. \tag{19}$$

It is clear that the first derivative matrices for all collocation points in (12) are still valid for the infinite element except the nodes at $\xi_1 = 1$.

(2) Five-seeds mapping

Same as four seed mapping, the edge of the right hand side $(\xi = 1)$ is mapped to an infinite place, as shown in Figure 3. The mapping functions are given as,

$$N_1 = -\frac{(1+\xi_1+\xi_2)(1-\xi_2)}{(1-\xi_1)}, \ N_2 = \frac{(1+\xi_1)(1-\xi_2)}{2(1-\xi_1)}, \ N_3 = \frac{(1+\xi_1)(1+\xi_2)}{2(1-\xi_1)}$$

$$N_4 = \frac{(-1+\xi_2-\xi_1)(1+\xi_2)}{(1-\xi_1)}, \ N_5 = \frac{2(1-\xi_2^2)}{(1-\xi_1)}. \tag{20}$$

Then their partial differentials respect to ξ and η are given as,

$$\frac{\partial N_1}{\partial \xi_1} = -\frac{(1-\xi_2)(2+\xi_2)}{(1-\xi_1)^2}, \ \frac{\partial N_2}{\partial \xi_1} = \frac{(1-\xi_2)}{(1-\xi_1)^2}, \ \frac{\partial N_3}{\partial \xi_1} = \frac{(1+\xi_2)}{(1-\xi_1)^2},$$

$$\frac{\partial N_4}{\partial \xi_1} = -\frac{(1+\xi_2)(2-\xi_2)}{(1-\xi_1)^2}, \ \frac{\partial N_5}{\partial \xi_1} = \frac{2(1-\xi_2^2)}{(1-\xi_1)^2}. \tag{21}$$

and

$$\frac{\partial N_1}{\partial \xi_2} = \frac{(2\xi_2+\xi_1)}{(1-\xi_1)}, \ \frac{\partial N_2}{\partial \xi_2} = -\frac{(1+\xi_1)}{2(1-\xi_1)}, \ \frac{\partial N_3}{\partial \xi_2} = \frac{(1+\xi_1)}{2(1-\xi_1)},$$

$$\frac{\partial N_4}{\partial \xi_2} = \frac{(2\xi_2-\xi_1)}{(1-\xi_1)}, \ \frac{\partial N_5}{\partial \xi_2} = -\frac{4\xi_2}{(1-\xi_1)}. \tag{22}$$

Two and three dimensional mapping and shape functions for different types of the infinite element used in the finite element method are catalogued in [14] by Marques. Zienkiewicz [6] presented an extensive survey of procedures used for finite element unbounded domain analysis, grouping them in accordance with the nature of the algorithm.
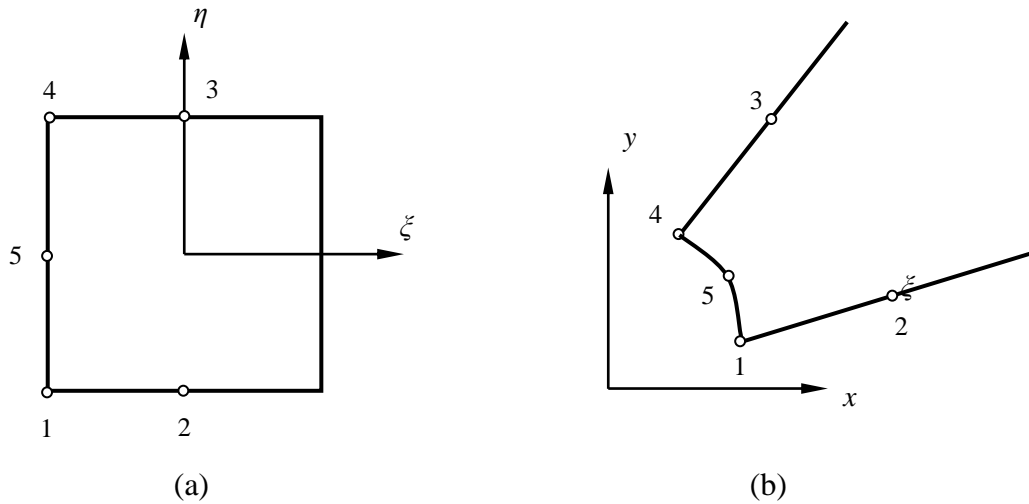

(a)   (b)

Figure 3. Five nodes mapping: (a) normalized domain; (b) physical domain.

4. Transient heat conduction in cutting/grinding process

Consider a schematic representation of the surface grinding process, as shown in Figure 4. A workpiece of contact length $2l$ and depth of cut a is observed moving with constant speed V horizontally. The average heat flux q_0 into the workpiece in the grinding process can be determined from,

$$q_0 = \frac{\varepsilon U a}{\tau} \tag{23}$$

where $\tau = 2l/V$ is interaction time, $l = \sqrt{da}/2$, where d is the wheel diameter, U is the specific grinding energy and ε is the fraction of this energy which is conducted as heat transfers into the workpiece. The factor ε can be obtained from a heat partition analysis proposed by Moulik *et al*. [10]. In the present paper, a moving band source of heat q_0 or linear variation of heat source is presented on a semi-infinite solid inclined at angle ϕ to its direction of movement with material disappearing as the heat source passes. The thermal modeling is presented by considering the grinding zone as a continuous band source of heat moving at the workpiece velocity. However, with large depths of cut/grinding the grinding zone becomes more inclined, as shown in Figure 4, and the inclined angle should therefore be taken into account. The geometrical arc length of contact between the wheel and the workpiece can be treated as a straight line of length $2l$, as shown in Figure 4. The inclination angle is given by, $\phi = \sin^{-1}(\sqrt{a/d})$.

The governing equation for two-dimensional transient heat conduction in isotropic and a continuously homogeneous media (Ω), with no internal heat source, is given by the following partial differential equation:

$$\kappa\left(\frac{\partial^2 u}{\partial x_1^2} + \frac{\partial^2 u}{\partial x_2^2}\right) - \rho c V \frac{\partial u}{\partial x_1} = \rho c \frac{\partial u}{\partial t}, \qquad \mathbf{x} \in \Omega, \ t > 0 \tag{24}$$

with the initial condition in the domain Ω and boundary condition on Γ conditions as follows,

$$
\begin{aligned}
u &= u_0(\mathbf{x}), & \mathbf{x} \in \Omega, \ t = 0 \\
\beta u + \gamma q_n &= f(\mathbf{x},t), & \mathbf{x} \in \Gamma, \ t > 0 \\
q_n &= -\kappa\left(\frac{\partial u}{\partial x_1} n_1 + \frac{\partial u}{\partial x_2} n_2\right)
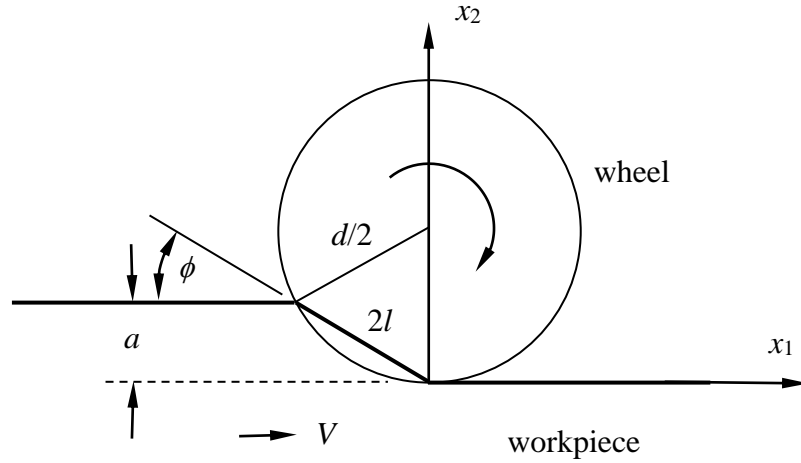\end{aligned}
\tag{25}
$$

Figure 4. Geometry of the wheel, workpiece and slant shear plane.

where u is temperature, κ is thermal conductivity, c is specific heat, ρ is mass density, t is time, $f(\mathbf{x},t)$ is given function, $\mathbf{x}$ is coordinate (x_1,x_2), (n_1,n_2) is unit normal outwards, β and γ are coefficients of the boundary. In a special case, the surface flux q_n from convective cooling losses can be written as,

$$q_n = h(u - u_\infty) \tag{26}$$

where h is surface heat transfer coefficient and u_∞ is ambient temperature, which is specified as zero in this paper.

Unlike the traditional meshless method, the physical domain is divided into a few blocks by using FBM. For stationary heat conduction, the term on the right-hand side of (24) does not exist. By applying the mapping technique and differential matrices in (24) for each block, we obtain,

$$\left(\mathbf{D}_1^2 + \mathbf{D}_2^2 - \alpha V\mathbf{D}_1\right)\mathbf{u} = \mathbf{0} \qquad\qquad \mathbf{x}_i \in \Omega \tag{27}$$

where $\alpha(=c\rho/k)$ is thermal diffusivity, temperature vector of nodal value $\mathbf{u} = \{u_1,u_2,...,u_M\}^T$, $M(=N \times N)$ is the number of nodes for each block. The boundary condition yields,

$$\beta u_i - \gamma\kappa\sum_{j=1}^{M}\left(d_{1ij}n_1^{(i)} + d_{2ij}n_2^{(i)}\right)u_j = f(\mathbf{x}_i) \qquad \mathbf{x}_i \in \Gamma \tag{28}$$

In this case with more than one block, the continuous conditions on the smooth interface except two ends (joints) between blocks I and II gives,

$$u^{(I)}(\mathbf{x}_i) - u^{(II)}(\mathbf{x}_i) = 0, \ q^{(I)}(\mathbf{x}_i) + q^{(II)}(\mathbf{x}_i) = 0. \qquad \mathbf{x}_i \in \Gamma_{\text{int}} \tag{29}$$

Γ_{int} indicates the interface. Furthermore, at the corner joint $\mathbf{x}$, both the temperature continuity conditions and point heat equilibrium should be considered as,

$$u^{(I)}(\mathbf{x}_Q) = u^{(II)}(\mathbf{x}_Q) = ... = u^{(X)}(\mathbf{x}_Q), \tag{30}$$

$$\sum_{Q=I}^{X} \left(q_x^{(Q)}(\mathbf{x}_Q)[\sin\theta_2^{(Q)} - \sin\theta_1^{(Q)}] - q_y^{(Q)}(\mathbf{x}_Q)[\cos\theta_2^{(Q)} - \cos\theta_1^{(Q)}] \right) = p(\mathbf{x}_Q) \tag{31}$$

where X indicates the number of blocks, $\theta_2^{(Q)}$ and $\theta_1^{(Q)}$ are the starting and ending angles at the joint for block Q and $p(\mathbf{x})$ is the total heat into the joint from outer surfaces A and B, as shown in Figure 5. By solving a set of $m \times N \times N$ linear algebraic equations from (27) to (31), here m is the number of block, the numerical solutions of temperature at each node can be determined.
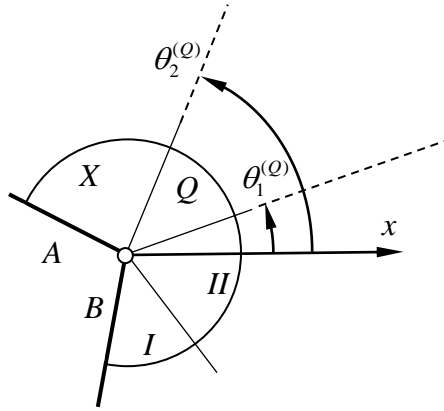
Figure 5. End of interface with starting and ending angles for each block, A and B are boundaries.

For transient heat conduction problems, there are two types of approaches, i.e. time domain and transform domain techniques. In general, by using the time domain technique, the finite difference method is applied. In this paper, the Laplace transformation is utilized due to the linearity of problem. Applying Laplace transform over both sides of (24) results in,

$$\rho c(s\tilde{u} - u_0) - \kappa\left(\frac{\partial^2\tilde{u}}{\partial x_1^2} + \frac{\partial^2\tilde{u}}{\partial x_2^2}\right) + \rho c V \frac{\partial\tilde{u}}{\partial x_1} = 0, \qquad \mathbf{x} \in \Omega \tag{32}$$

with the boundary condition,

$$\beta\widetilde{u} + \gamma\widetilde{q}_n = \widetilde{f}(\mathbf{x},s), \qquad\qquad\qquad \mathbf{x}\in\Gamma \qquad\qquad (33)$$

where the Laplace transform is defined as following,

$$\widetilde{F}(s) = \int_0^\infty F(t)e^{-st}dt, \qquad\qquad\qquad\qquad\qquad (34)$$

where s is Laplace transform parameter. Following the same numerical procedure for stationary problem by using the mapping technique in (32) results in,

$$\left[\alpha s\mathbf{I} - \left(\mathbf{D}_1^2 + \mathbf{D}_2^2\right) + \alpha V\mathbf{D}_1\right]\widetilde{\mathbf{u}} = \alpha\mathbf{u}_0 \qquad\qquad \mathbf{x}\in\Omega \qquad\qquad (35)$$

for each block, where $\mathbf{I}$ is the unit diagonal matrix. The boundary conditions yield,

$$\beta\widetilde{u}_i - \gamma\kappa\sum_{j=1}^M \left(d_{1ij}n_1^{(i)} + d_{2ij}n_2^{(i)}\right)\widetilde{u}_j = \widetilde{f}(\mathbf{x}_i,s) \qquad\qquad \mathbf{x}_i\in\Gamma \qquad\qquad (36)$$

By changing u in the stationary case with $\widetilde{u}$, one can obtain continuous conditions between two blocks at the interface including corner joints in the transformed domain for specified Laplace parameter s. A simple and accurate method proposed by Durbin [29] is adopted in this paper following two steps: (1) selecting $(K+1)$ samples in the transformation space $s_k, k = 0,1,...,K$, the transformed variables $\widetilde{u}(\mathbf{x}_i, s_k)$ should be determined by FBM; (2) computing temperature $u(\mathbf{x}_i,t)$ in the time domain by,

$$u(t) = \frac{2e^{\eta t}}{T}\left[-\frac{1}{2}\widetilde{u}(\sigma) + \sum_{k=0}^K \mathrm{Re}\left\{\widetilde{u}\left(\sigma + 2k\pi i/T\right)e^{2k\pi i/T}\right\}\right], \qquad\qquad (37)$$

where the Laplace parameter is selected $s_k = \sigma + 2k\pi i/T$, in which $i = \sqrt{-1}$. Obviously, there are two free normalised parameters in s_k: σ and T. The selection of parameters T depends on the observing period in the time domain. In the following examples, all variables are normalised with dimensions of unit for the convenience of analysis.

5. Numerical analysis

A two-dimensional heat transfer model is considered with its boundary conditions schematically illustrated in Figure 4. For the sake of analysis convenience, three free dimensionless parameters are introduced; dimensionless heat source half-width $L = Vl/2\alpha$, the dimensionless convective cooling coefficient $H = 2h\alpha/\kappa V$ and inclination angle ϕ. In general,

the normalized temperature $\bar{u} = \pi \kappa V u / 2\alpha q_0$ in the field depends on the three dimensionless parameters, i.e. L, H and ϕ. The dimensionless temperature $\bar{u}$ is used primarily for ease of comparison with other solutions [5,9] and all lengths are normalized to the half length of contact zone l. From the geometry shown in Figure 4, the depth and width of the workpiece are selected as $h_1 = w_1 = w_3$, and $h_2 = h_1 - 2l \sin \phi$, $w_2 = 2l \cos \phi$. Same conclusion [9] has been found that the distances of $h_1 / l = 4$ and $h_1 / l = 5$ did not show any appreciable difference in computed temperatures. Therefore, the depth of the region was chosen as $h_1 = 4l$ in this numerical modelling. The spacing of nodal points along the surface is varied in order to give higher resolution near the trailing edge of the heat source as Chebyshev's roots, as

$$\xi_\alpha^{(k)} = \cos \frac{\pi(k-1)}{N_\alpha}, \quad k = 1, 2, ..., (N_\alpha + 1) \tag{38}$$
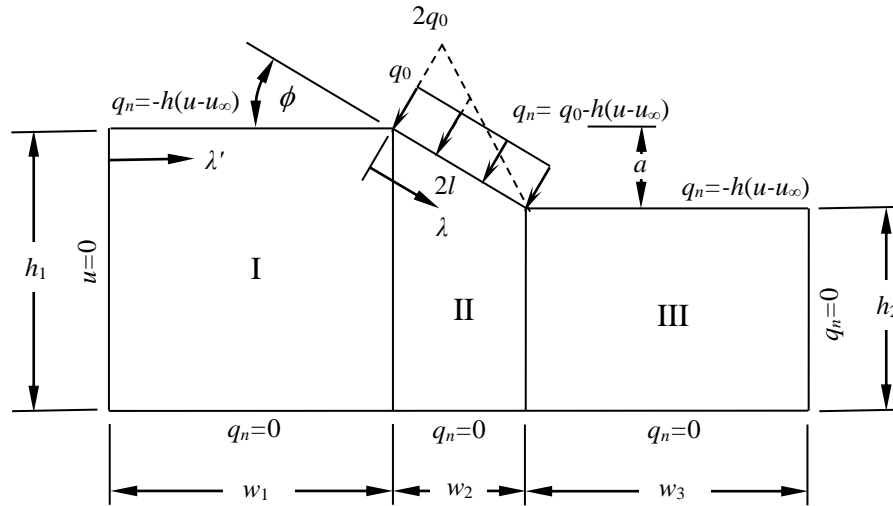
Figure 6. Model of cutting/grinding process using three blocks and boundary conditions.

and the node number $N_1 = N_2 = 20$, as it is observed that the difference is ignorable for $N_1 = N_2 = 10$. All computations are performed with double precision on a Lenovo-PC. The numerical solutions of the normalized temperature on the top surface of the workpiece versus λ'/l when $H = \phi = 0$ by the finite block method are smooth for different dimensionless parameter L shown in Figure 7. Contact zone is $4 \leq \lambda'/l \leq 6$. Comparison with the Jaeger's

analytical solution [5] and the Finite Element Analysis (FEA) [14] shows excellent agreement for these solutions of normalized temperature. Furthermore, no oscillation (instability) is observed by using FBM at all. However, the oscillations phenomenon using FEM was reported by Dawson and Malkin [9] and therefore many more elements would be required in his work.
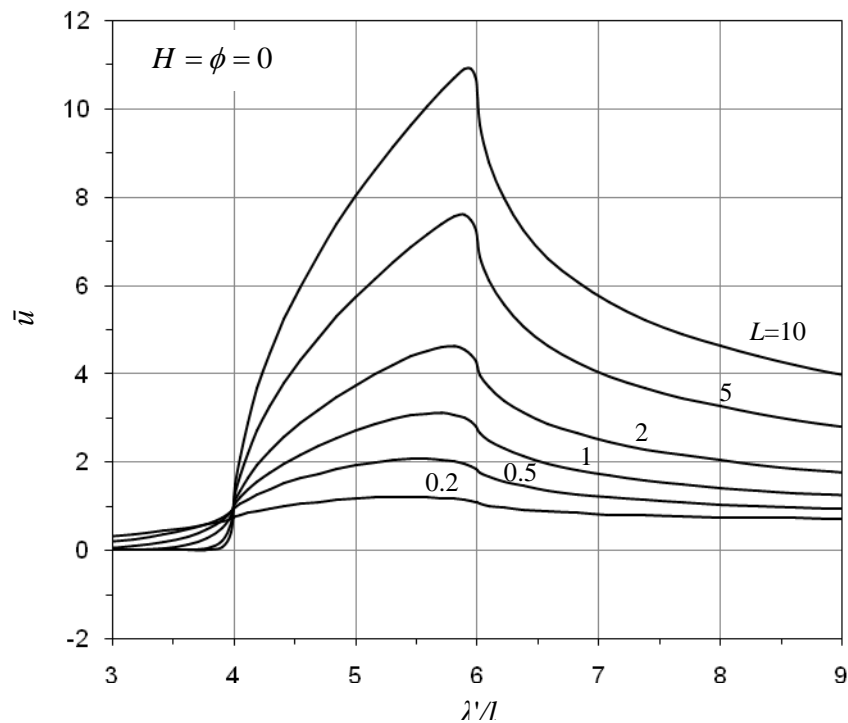

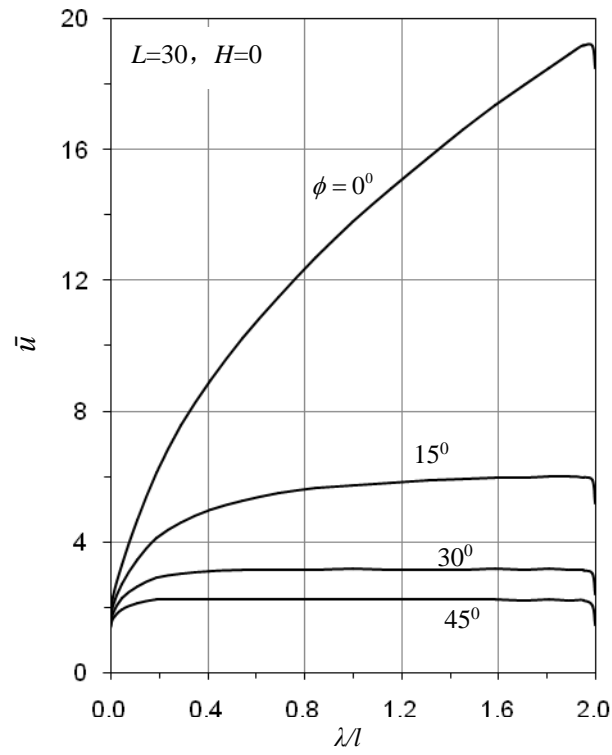Figure 7. Temperature distribution on the top surface of the workpiece with different dimensionless parameter *L*.

Figure 8. Temperature distribution on the shear plane with different inclind angle.
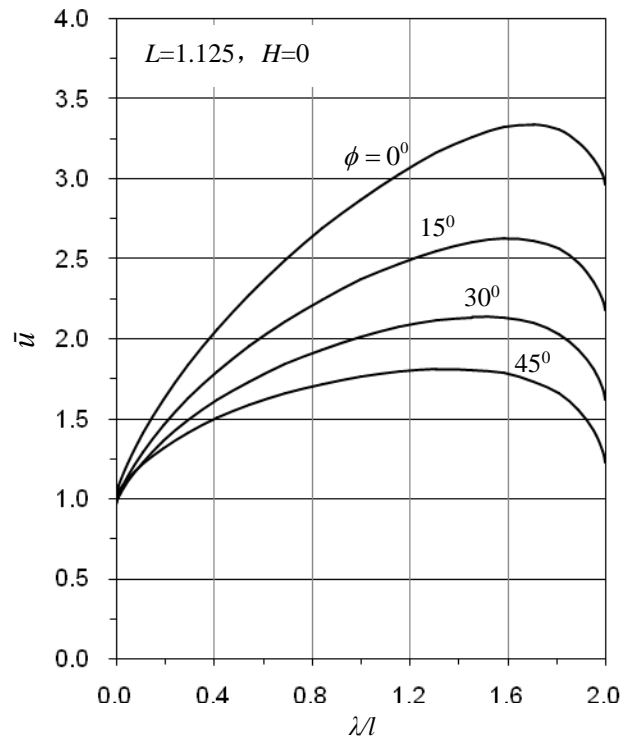
Figure 9. Temperature distribution on the shear plane for different inclind angle.
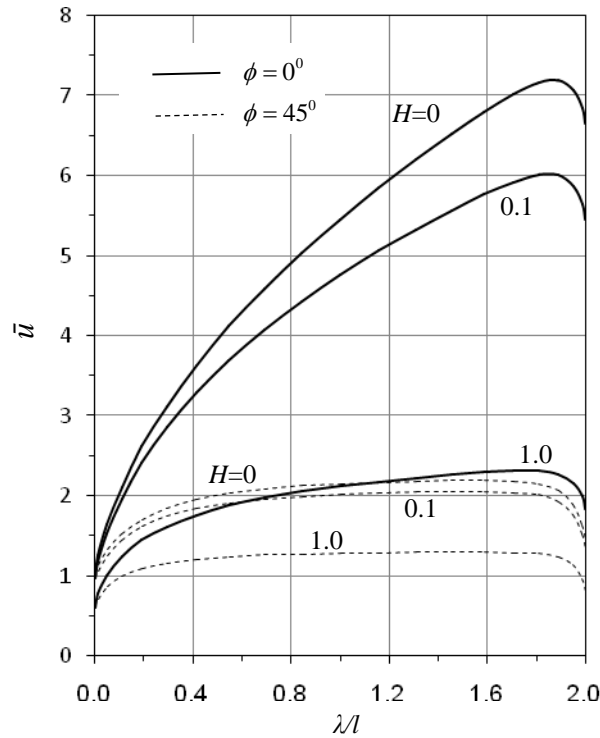
Figure 10. Temperature distribution on the shear plane with different cooling parameters, *L*=4.5.

The effect of the inclination angle ϕ on the temperature distribution is observed in the example. The temperature in the contact zone is shown in Figures 8 and 9 for a large and a small value of *L* (*L*=30 and *L*=1.125) respectively. In addition, the combined influence of the inclination angle ϕ and surface cooling (*H*) on the surface temperature distribution within the band source is observed. Figure 10 shows the distribution of surface temperature versus the location λ/l for different cooling parameter *H* and an intermediate value of *L*=4.5 when ϕ is chosen as 0^0 and 45^0 respectively. It is clear that the surface cooling parameter *H* has much bigger influence at $\phi = 0^0$ than at ϕ=45^0. Contours of the normalized temperature around the contact zone are plotted in Figure 11 for different free parameter *L* and inclined angle ϕ and other two free parameters including: (1) *H*=0.1, ϕ=0 in Figures 11(a)-(d); and (2) *H*=0.1, *L*=4.5 in Figures 11(e)-(h). It is apperent that at low values of *L*, conduction carries heat well into the workpiece. As *L* increases, heat does not propagate before it is swept away by the increased velocity of the workpiece. Similarly, with increase of the inclind angle ϕ, the heat does not propogate into the workpiece. In addition, a linear variation model of heat flux across the

contact zone (shear plane) is shown in Figure 4 with a dashline, in which the heat source starts from zero on the bottom of the shear plane to maximum value of $2q_0$ on the top surface. The temperature distribution is shown in Figure 12 for a different inclination angle ϕ, when L=30 and H=0 respectively. To demonstrate the difference between these two models of heat source distribution (uniform and linear distributions of heat flux), the numerical results with uniform model are plotted in the same figure for comparison. It is very obvious that the differences between them are significant.
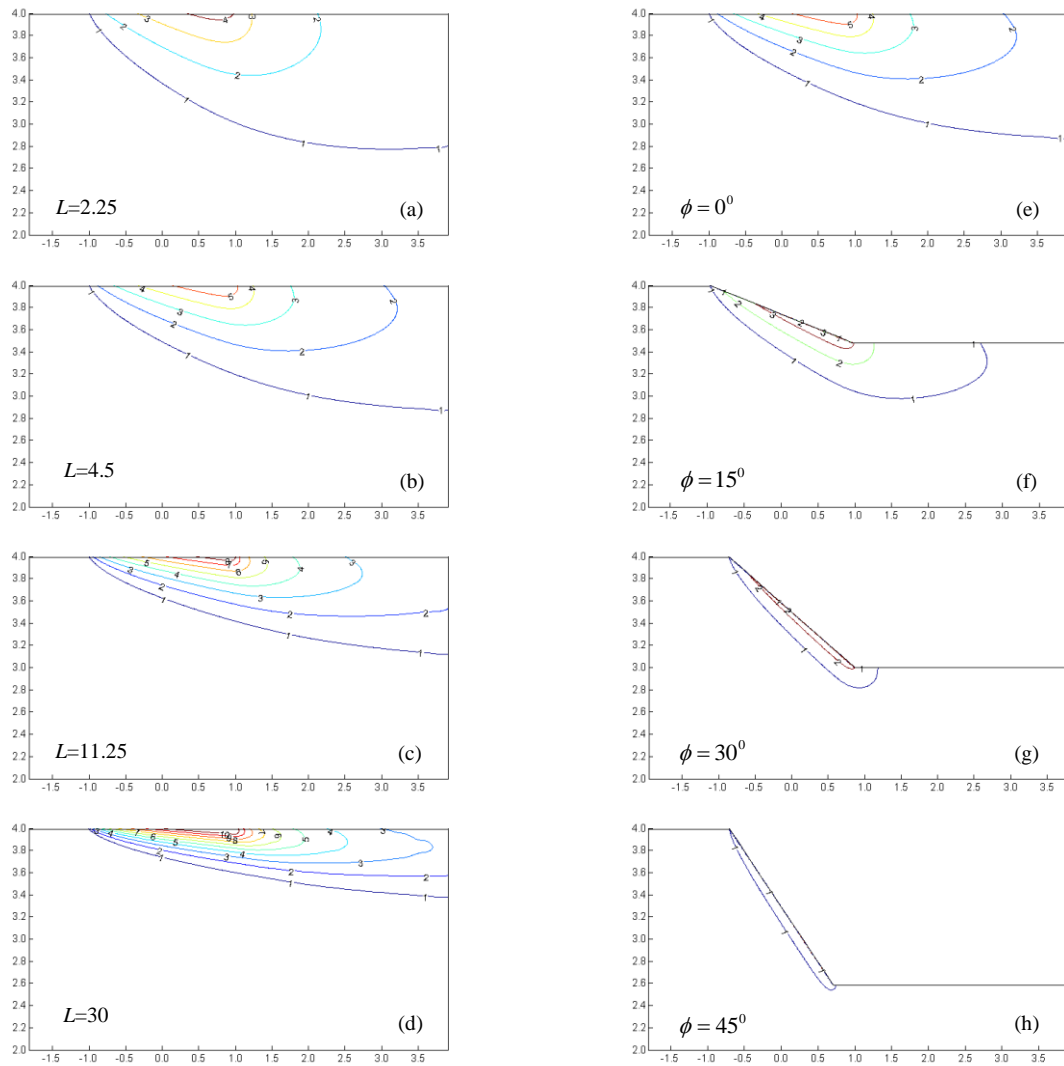
Figure 11. Contours of the normalized temperature centred at the middle of contact zone for different parameter L and angles of the contact surface ϕ, where (a)-(d): H=0.1, ϕ=0; (e)-(h): H=0.1, L=4.5.
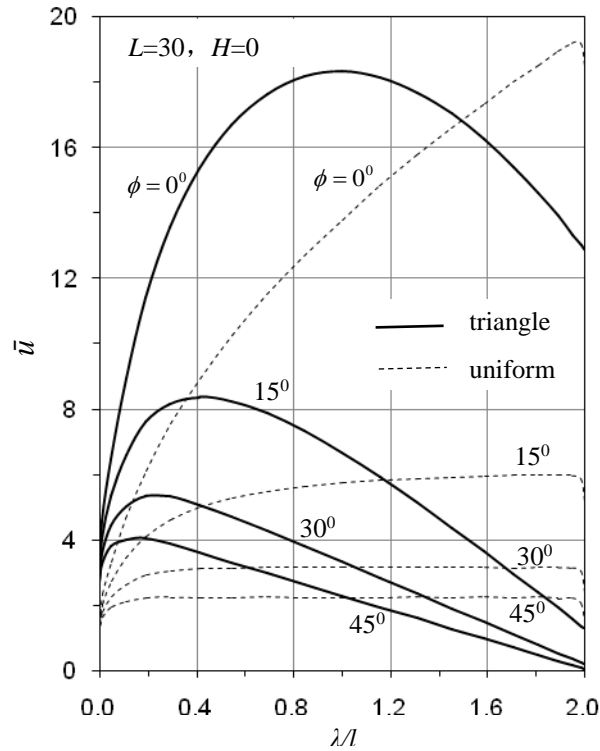
Figure 12. Temperature distribution on the top of the workpiece with different inclination angle.

In order to observe the degrees of accuracy and convergence, the finite element analysis commercial software ABAQUS is employed. Same modelling as shown in Figure 13 is considered with the speed $V = 0$ and inclination angle $\phi = 15^0$. Fine mesh of FEM is shown in Figure 13. The results of temperature distribution $\bar{u} = \kappa u / q_0 l$ on the shear zoon are presented in Figure 14(a) for FEM and Figure 14(b) for FBM with different node densities. Element type DCD4 is used for ABAQUS. For FEM with coarse mesh, i.e. the total number of node $N = 60$, the degree of accuracy is poor. Reasonable solutions can be obtained when $N = 207$. Seeing from Figures 14(a)(b), it is clear that the results given by FBM is more accurate than those by FEM with same node number. When the node number $N \geq 768$ for FBM, it is hard to see the difference between accurate solution by FEM with high density of node ($N = 12765$). However, the CPU time used by ABAQUS is about 0.1 second and 5 second used by FBM with desktop PC Intel(R) Core(TM)i7-4770S.
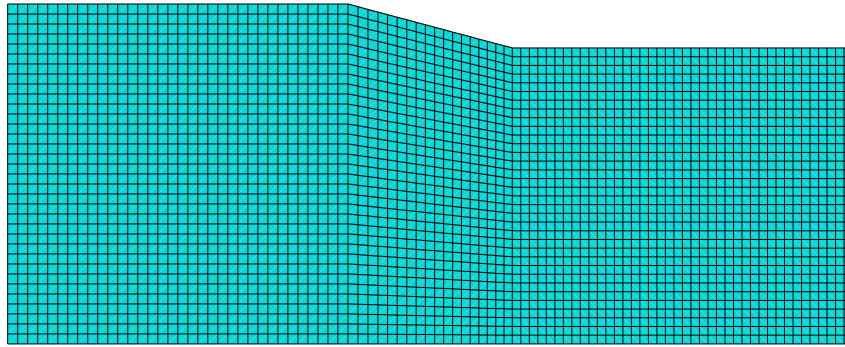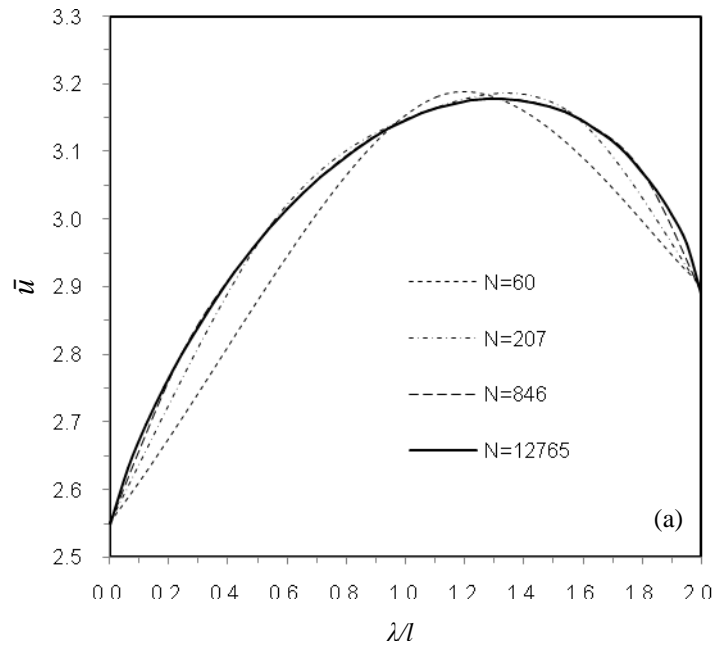
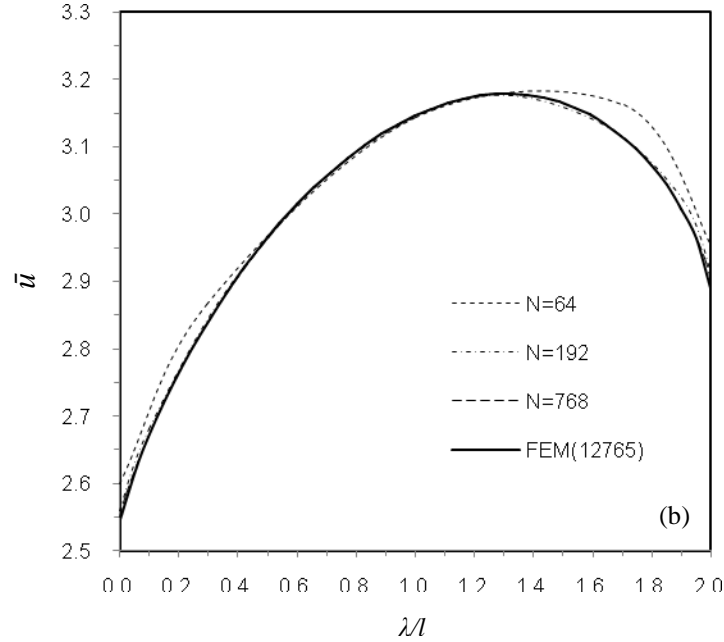Figure 13. Finite element mesh used in ABAQUS.

Figure 14. Distribution of temperature along the shear zoon: (a) numerical results by ABAQUS; (b) nmerical results by FBM.

In order to consider the accuracy of the FBM, comparison has been made with numerical solution by Gonzalez-Santander [15] for different flux densities on the cutting surface. Three flex modes are considered as

(1) *Linear profile.* The linear heat flux profile is given by

$$q(\xi) = q_0(1 - \lambda/l) .$$ (39)

(2) *Triangular profile.* The triangular heat flux profile is given by

$$q(\xi) = \begin{cases} \dfrac{2q_0}{1+\beta}\left(1+\dfrac{\lambda}{l}\right) & -1 \le \xi \le \lambda l \\ \dfrac{2q_0}{1-\beta}\left(1-\dfrac{\lambda}{l}\right) & \lambda l \le \xi \le 1 \end{cases} .$$ (40)

(3) *Parabolic profile.* The parabolic heat flux profile is given be

$$q(\xi) = \frac{3q_0}{4}(1 - \lambda/l)^2 .$$ (41)

where the normalised coordinate ($-1 \le \lambda/l \le 1$) is established on the cutting surface. The temperature distribution on the cutting surface for linear, triangular and parabolic heat flux profiles are plotted in Figure 15 respectively. The dimensionless parameter $L=10$ for all graphs

and dimensionless parameter $\beta = -0.6$. The excellent agreement with the results in [15] are achieved obviously.
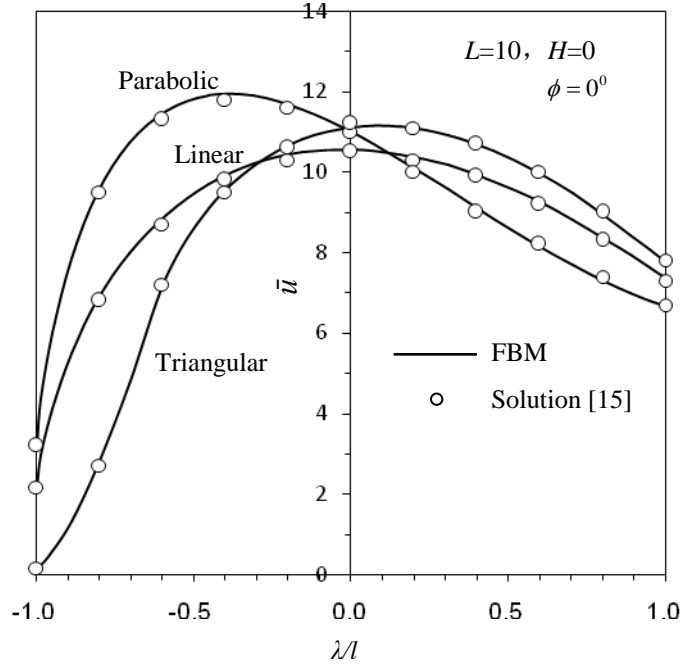

Figure 15. Temperature distribution on the top of the workpiece with different heat flux profiles.

For transient heat conductions, the time t is normalized to $t_0 (= \rho c l^2 / \kappa)$. Two free parameters are chosen as $\sigma = 5/T$. The maximum number of sample points in the Laplace transform domain is selected as $K = 200$ in this example. The heat flux on shear plane is time dependent as $q(t) = q_0 H(t)$, here $H(t)$ is the Heaviside function. The variation of normalized temperature at the middle of the shear plane (contact zone) with uniform heat source and zero initial condition ($\mathbf{u}_0 = \mathbf{0}$) versus the normalized time $\bar{t}(= t/t_0)$ for various of parameter L is shown in Figure 16, here $H = \phi = 0$. In this case, the observing time is $T = 60$ in the Durbin inversion method. It is clear that the temperature is convergent to the stationary value in a short time. However, the time of convergence depends on the dimensionless parameter L significantly, i.e. the smaller of the parameter L, is the much shorter of the time to the stationary state would be. Furthermore, Figure 17 sketches the distribution of surface temperature for different normalized time intervals of 0.5 with $L = 1.125$, $H = \phi = 0$ and

observing time $T = 10$. Apparently, the convergence to the stationary state can be achieved when $\bar{t} > 3$.
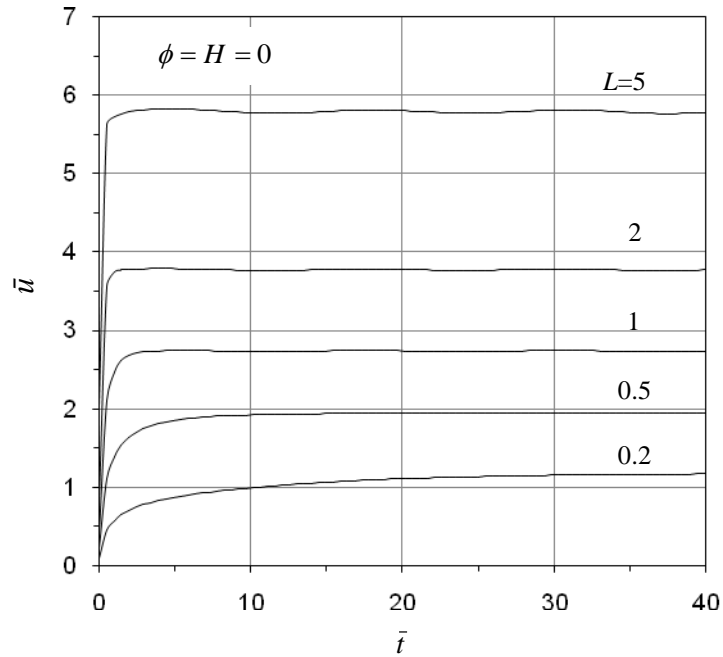

Figure 16. Normalized temperature variation versus the normalized time at the middle of contact zone with different parameter L of velocity.
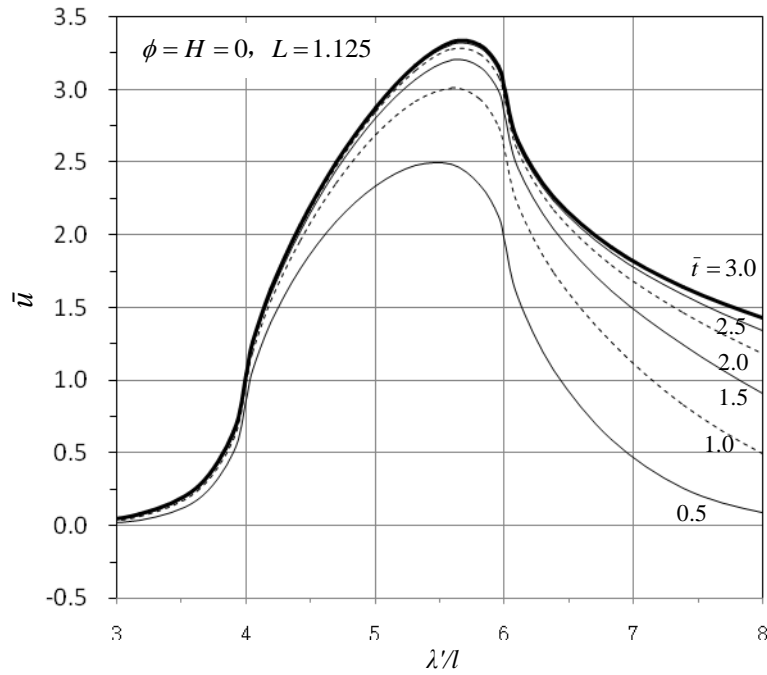
Figure 17. Temperature distribution on the top of the workpiece with normalized time intervals.

The same problem shown in Figure 6 is reanalyzed by the use of infinite element. In this modeling, block III is replaced with an infinite element as shown in Figure 16. To observe the convergence of the temperature on the surface of the workpiece, the boundary condition is changed on the bottom and on the right-hand side ($u = 0$). The node distribution is shown in Figure 19 with an infinite element III, where the node number $N_1 = N_2 = 10$ for each block. The numerical solution of the normalized temperature on the top surface of the workpiece versus λ'/l ($0 \le \lambda'/l \le 50$) is shown in Figure 18, when $H = \phi = 0$ for different dimensionless parameter L, where the node number $N_1 = N_2 = 30$. The grinding zone is located in the region of $4 \le \lambda'/l \le 6$. By observing the results in Figure 20, the excellent agreement with three normal blocks is achieved apparently for the temperature in the region $0 \le \lambda'/l \le 9$ apart from a small region near the end of block III, i.e. $\lambda'/l = 10$ (truncation of the domain). However, by using the infinite element, the temperature can be obtained for an unbounded domain.
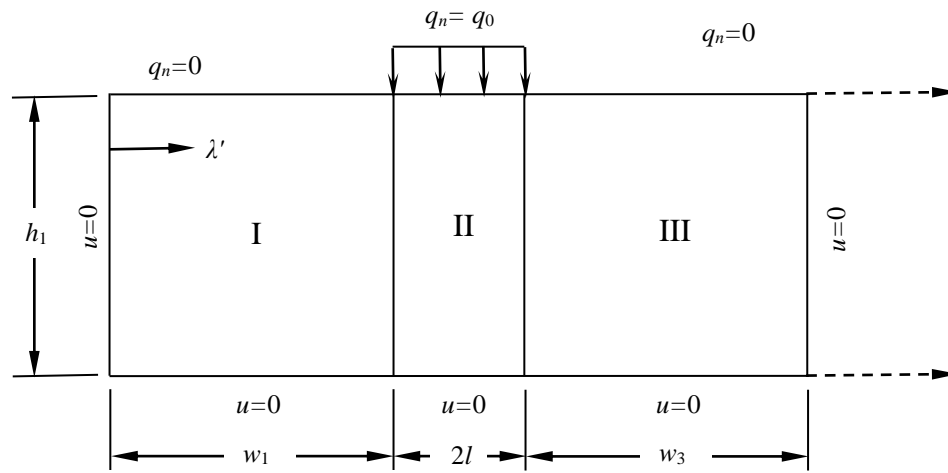
Figurer 18. Model of cutting/grinding process with two blocks, an infinite element and boundary conditions
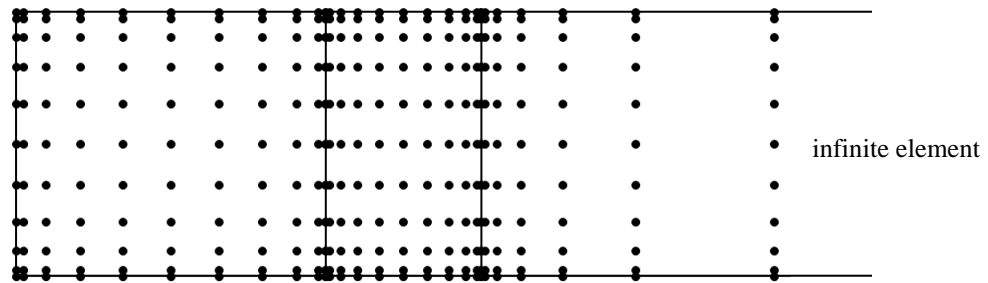

Figure 19. Nodal distribution in the physical domain: two blocks and one infinite element.
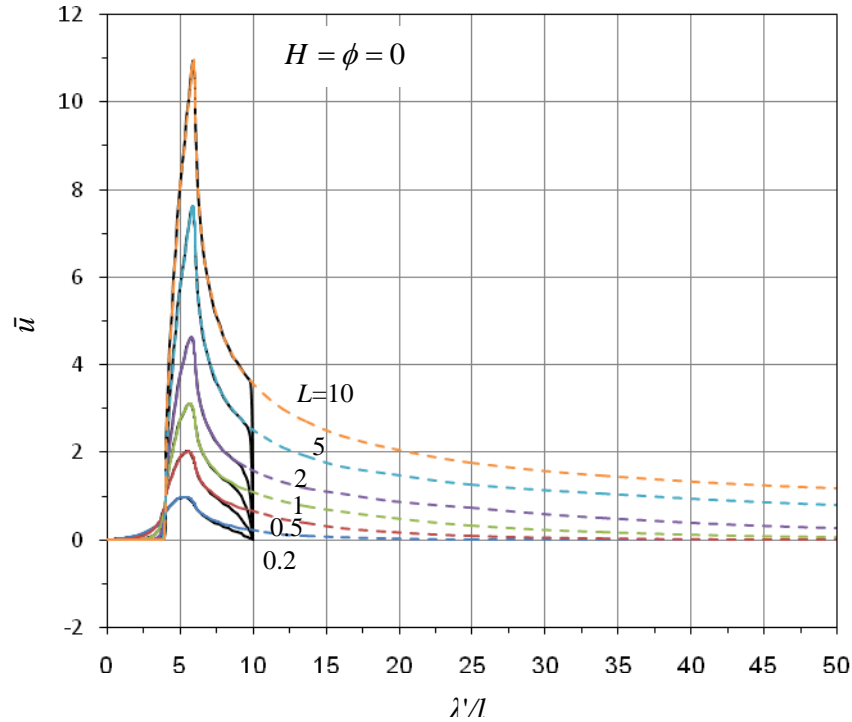
Figure 20. Temperature distributions on the surface both for truncated domain and unbounded domain.

Finally one more complicated problem is considered, i.e. the influence on the temperature distribution from the chip in the cutting procedure is observed. The geometry of modeling is shown in Figure 21. A workpiece with chip ABCD moves with constant speed V horizontally. The heat source density q_0 is uniformly distributed along the shear zoon AB. The node number $N_1 = N_2 = 16$ for each block, the slant angle $\phi = 15^0$ and all other dimensions are specified in the beginning of this section. When the speed $V = 0$, the distribution of temperature along the shear zoon AB by FBM is presented in Figure 22 and comparison with FEM is shown in the same figure, where the temperature is normalized $\bar{u} = \kappa u / q_0 l$ (node number is 3072). To verify the convergence of this method, the relative average error is found less than 0.01% with higher density of node. With non-zero velocity of motion, the numerical solutions of the normalized temperature $\bar{u} = \pi \kappa V u / 2\alpha q_0$ and flux density $\bar{q} = q_n^{II} / q_0$ of block II on the shear zoon AB versus λ / l are shown in Figures 23 and 24 for different of dimensionless parameter

L respectively. It is evident that the flux densities of $\bar{q}$ along the shear zoon AB are more than 80% for all cases.
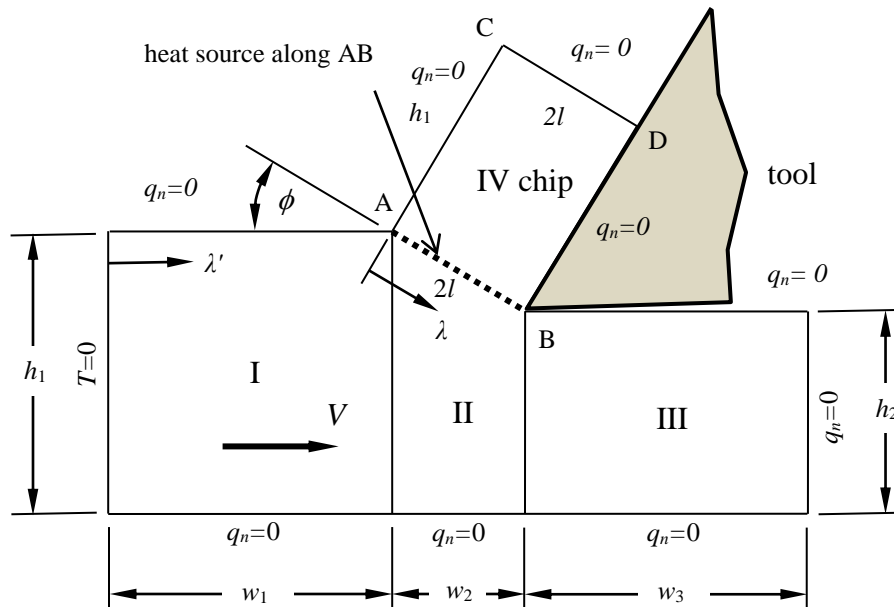

Figure 21. Finite block modelling of workpiece with chip and heat source along AB.
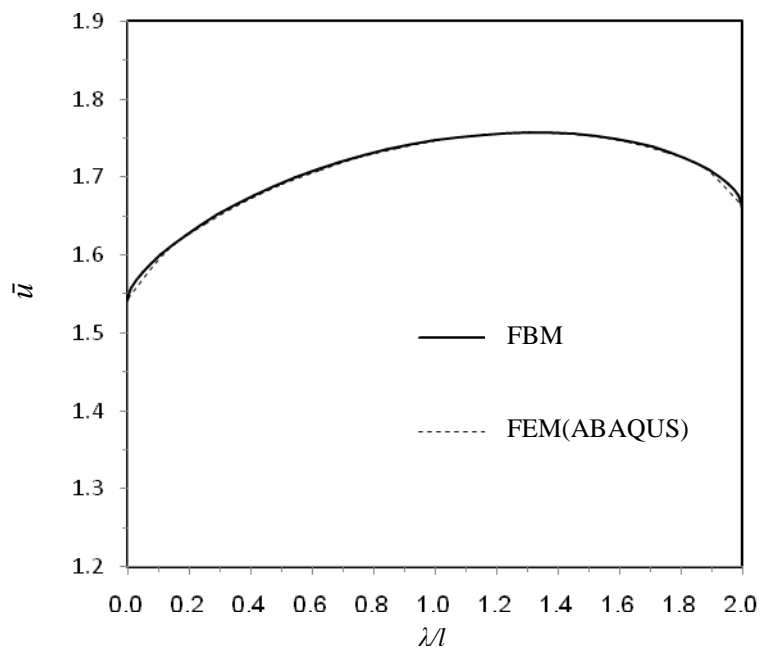

Figure 22. Distributions of temperature along the shear zoon by FBM and FEM.
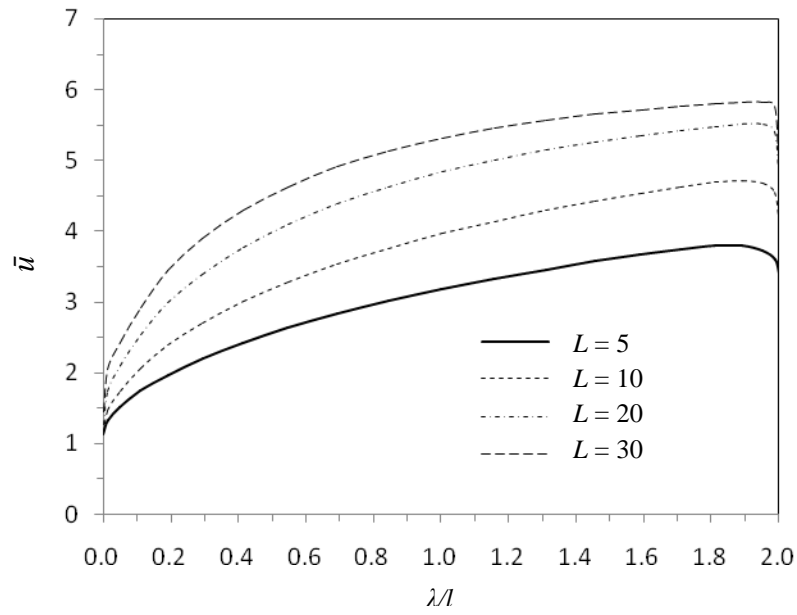
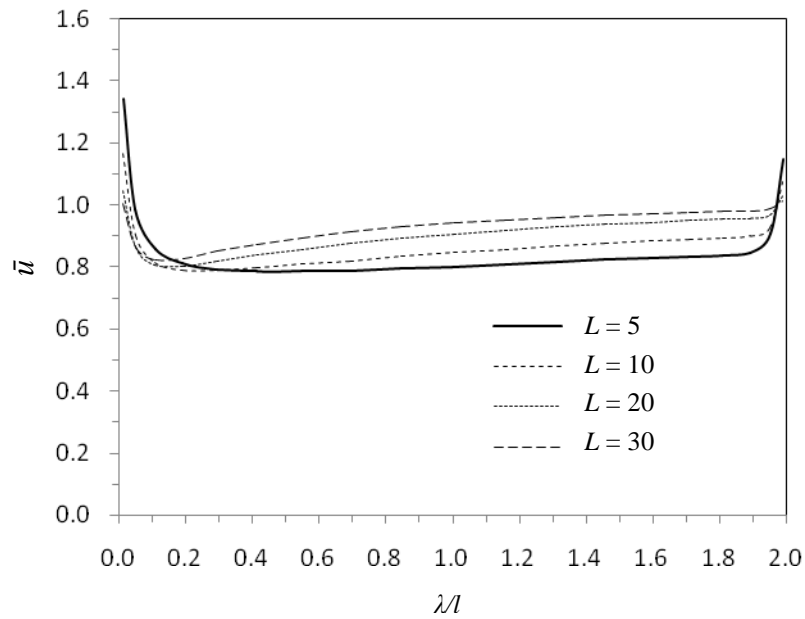Figure 22. Temperature distribution versus the local coordinate λ/l and different dimensionless parameter *L*.

Figure 22. Flux density of block II versus the local coordinate λ/l and different dimensionless parameter *L*.

6. Conclusion

A meshless method, called the finite block method, was developed to study the heat transfer problem for metal cutting/grinding thermal modelling of an inclined band source of heat moving along the surface of a semi-infinite solid. The finite block method was proposed for general heat transfer problems generated from the metal cutting/grinding process. This method considered the governing equations in the strong form and the system equations are formulated with partial differential matrices from the equilibrium equations, boundary conditions and continuous conditions for all blocks. As the higher order of the partial differentials are evaluated by the Lagrange series with an easy mapping technique, the computational effort is reduced significantly compared to other meshless methods. In addition, using the mapping technique with infinite elements the system equations in strong form were formulated with the first order partial differential matrices from the equilibrium equations and boundary conditions for the unbounded domain. The stationary and transient temperature field were obtained by solving a set of linear algebraic equations. The results of this analysis were presented in terms of three dimensionless parameters including L, H and ϕ, and these results can be applied to compute the temperatures on the shear plane and the grinding surface. This method can be extended easily to any type of partial differential equations, including stress analysis of metal cutting/grinding problems.

Acknowledgement

References

[1]   Brinksmeier E, Aurich JC, Govekar E, Heinzel C, Hoffmeister HW, Klocke F, Peters J, Rentsch R, Stephenson DJ, Uhlmann E, Weinert K, Wittmann M. Advances in Modeling and Simulation of Grinding Processes. CIRP Annals - Manufacturing Technology 2006; 55(2): 667-696.

[2]   Doman DA, Warkentin A, Bauer R. Finite element modeling approaches in grinding. International Journal of Machine Tools and Manufacture 2009; 49(2): 109-116.

[3]   Komanduri R,Hou ZB. Thermal modeling of the metal cutting process. International Journal of Mechanical Sciences 2000; 42(9): 1715-1752.

[4]   Jen TC, Lavine AS. A variable heat flux model of heat transfer in grinding: model development. Journal of Heat Transfer 1995; 117(2): 473-478.

[5]   Jaeger JC. Moving sources of heat and the temperature at sliding contacts. J. Proc. Roy. Soc. NSW. 1942; 76: 203-224.

[6]   Mahdi M,Zhang LC. The finite element thermal analysis of grinding processes by ADINA. Computers & Structures 1995; 56(2): 313-320.

[7]   Shen B, Shih AJ, Xiao GX. A heat transfer model based on finite difference method for grinding. Journal of Manufacturing Science and Engineering 2011; 133(3): 031001-1-031001-10.

[8]   Wang XZ, Yu TB, Sun X, Shi Y, Wang WS. Study of 3D grinding temperature field based on finite difference method: considering machining parameters and energy partition. The International Journal of Advanced Manufacturing Technology 2016; 84(5): 1-13.

[9]   Dawson PR, Malkin S. Inclined moving heat source model for calculating metal cutting temperatures. Journal of Engineering for Industry 1984; 106: 179-186.

[10]   Moulik PN, Yang HTY, Chandrasekar S. Simulation of thermal stresses due to grinding. International Journal of Mechanical Sciences 2001; 43(3): 831-851.

[11]   Gu RJ, Shillor M, Barber GC, Jen T. Thermal analysis of the grinding process. Mathematical and Computer Modelling 2004; 39(9): 991-1003.

[12]   Anderson D, Warkentin A, Bauer R. Comparison of numerically and analytically predicted contact temperatures in shallow and deep dry grinding with infrared measurements. International Journal of Machine Tools and Manufacture 2008; 48(3): 320-328.

[13] Parente MPL, Jorge RMN, Vieira AA, Baptista AM. Experimental and numerical study of the temperature field during creep feed grinding. The International Journal of Advanced Manufacturing Technology 2012; 61(1-4): 127-134.

[14] Li J, Li JCM. Temperature distribution in workpiece during scratching and grinding. Materials Science and Engineering A 2005; 409:108-119.

[15] Gonzalez-Santander JL. Maximum temperature in dry surface grinding for high peclet number and arbitrary heat flux profile. Mathematical Problems in Engineering 2016: 1-9.

[16] Belytschko T, Krogauz Y, Organ D, Fleming M, Krysl P. Meshless methods; an over view and recent developments. Comput Meth Appl Mech Eng 1996;139:3-47.

[17] Sladek J, Sladek V, Zhang Ch. Transient heat conduction analysis in functionally graded materials by the meshless local boundary integral equation method. Comput. Material Science 2003; 28: 494-504.

[18] Sladek V, Sladek J, Zhang Ch. Local integro-differential equations with domain elements for the numerical solution of partial differential equations with variable coefficients. Journal of Engineering Mathematics 2005; 51: 261-282.

[19] Li HN, Yu TB, Zhu LD, Wang WS. Analysis of loads on grinding wheel binder in grinding process: insights from discontinuum-hypothesis-based grinding simulation. The International Journal of Advanced Manufacturing Technology 2015; 78(9): 1943-1960.

[20] Shimizu J, Zhou LB, Eda H. Simulation and experimental analysis of super high-speed grinding of ductile material. Journal of Materials Processing Technology 2002; 129(1): 19-24.

[21] Nguyen TA,Butler DL. Simulation of precision grinding process, part 1: generation of the grinding wheel surface. International Journal of Machine Tools and Manufacture 2005; 45(11): 1321-1328.

[22] Nguyen TA,Butler DL. Simulation of surface grinding process, part 2: interaction of the abrasive grain with the workpiece. International Journal of Machine Tools and Manufacture 2005; 45(11): 1329-1336.

[23]   Li M, Wen PH. Finite block method for transient heat conduction analysis in functionally graded media. International Journal For Numerical Methods in Engineering 2014; 99(5): 372-390.

[24]   Wen PH, Cao P, Korakianitis T. Finite Block Method in elasticity. Engineering Analysis With Boundary Elements 2014; 46: 116-125.

[25]   Li M, Lei M, Munjiza A, Wen PH. Frictional contact analysis of functionally graded materials with Lagrange finite block method. International Journal For Numerical Methods in Engineering 2015; 103(6): 391-412.

[26]   Li M, Meng LX, Hinneh P, Wen PH. Finite block method for interface cracks. Engineering Fracture Mechanics 2016; 156: 25-40.

[27] Wood WL. On the finite element solution of an exterior boundary value problem. *Int. J. Numer. Methods Eng.* 1976; 10: 885-891.

[28] Bettess P, Zienkiewicz OC. Diffraction and refraction of surface waves using finite and infinite elements. *Int. J. Numer. Methods Eng.* 1977; 11: 1271-1290.

[29] Durbin F. Numerical inversion of Laplace transforms: an efficient improvement to Dubner and Abate's method. Comput. J. 1974; 17 (4): 371–376.